Original Article

Energy-Efficient Cognitive MIMO Framework for Bedridden Patient Monitoring Using Deep Learning

G. Kalaimagal[1], M.S.Vasanthi[2]

[1,2]*Department of Electronics and Communication Engineering, SRM Institute of Science and Technology, Kattankulathur, Tamilnadu, India.*

[1]*Corresponding Author: kalaimag@srmist.edu.in*

Abstract - In this article, a new approach for monitoring the temperature of bedridden patients is presented, which continues to pose a challenge. To solve this problem, a proposed Optimized MSE and Energy Efficiency Enhancement (Opti-MSEEE) algorithm, which uses underlay cognitive Multiple-Input Multiple-Output (MIMO) to send thermal images and a U-Net method to restore the images. This proposed work facilitates reliable thermal image transmission, restoration, and temperature prediction using an underlay cognitive MIMO system. The work incorporates a closed-form mathematical model based on the Optimized MSE and Energy Efficiency Enhancement (Opti-MSEEE) algorithm, which jointly minimizes the Sum Minimum Mean Square Error (Sum-MSE) and maximizes Energy Efficiency (EE) for transmission strategies. Simulation findings show that Opti-MSEEE outperforms other schemes, which proves that it has better EE. To ensure image integrity, the work integrates a deep learning–based dynamic channel selection mechanism at the Cognitive Base Station (CBS) transmitter and employs a lightweight deep learning model, the Nonlinear Activation Free Network–lite version (NAFNet-lite), at the receiver for accurate image restoration. Comparative evaluation shows that NAFNet-lite achieved the highest Peak Signal-to-Noise Ratio (PSNR) of 31.2 dB and a Structural Similarity Index Measure (SSIM) of 0.794. Crucially, the deep learning model preserves thermal consistency, maintaining maximum and minimum temperatures closest to the original values, which is essential for diagnostic reliability. The full proposed work, the Thermal Image Cognitive Radio (TMCR) framework, was tested and confirmed using a specialized Raspberry Pi-based hardware testbed. Experimental results confirm that the reconstructed thermal images preserve fine structural details and accurate temperature information, highlighting the framework's suitability for resource-constrained medical thermal image applications.

Keywords - Underlay cognitive, Energy Efficiency, Peak Signal-to-Noise Ratio, Sum Minimum Mean Square Error, Structural Similarity Index Measure.

1. Introduction

Individuals who are confined to bed for prolonged periods often experience poor blood circulation and tissue damage, which leads to complications such as pressure ulcers, deep tissue injuries, inflammation, and tissue necrosis. These conditions make life less comfortable and significantly increase healthcare costs, highlighting the need to identify at-risk individuals early and maintain updated monitoring. However, conventional assessment methods remain limited by subjectivity, diagnostic delays, and periodic evaluations. To overcome these limitations, Cognitive Radio (CR) systems provide reliable and energy-efficient data transmission for distributed sensing in healthcare indoor/outdoor environments [1]. When integrated with embedded systems, CR enables real-time health monitoring and efficient utilization of network resources. Thermal imaging enhances diagnostic capability by capturing temperature variations associated with tissue abnormalities [2]. Low-latency and distortion-free wireless transmission helps preserve clinically relevant thermal information. Accurate medical interpretation depends on precise detection of temperature gradients [3]. Color-mapping palettes such as ironbow, arctic, and grayscale enhance contrast and highlight subtle thermal variations, supporting accurate clinical analysis. However, maintaining these palettes during underlay CR transmission remains challenging due to dynamic spectrum access and interference [4]. This work proposes a Thermal Medical Cognitive Radio (TMCR) framework that combines CR-based spectrum management with deep learning-based thermal image restoration to achieve reliable, energy-efficient, and clinically accurate medical image transmission.

2. Related Work

This study examines approaches for EE management and image restoration. Several existing EE works employs Lagrange multipliers for convex optimization problems [5], in

energy systems the convex problems satisfies the Karush–Kuhn–Tucker (KKT) conditions [7]. Alternate methods were used to investigate the EE in the non-convex optimization problems. The fractional programming for joint temporal power allocation [6] to improve energy utilization while preserving image pixels. To solve fractional programming problems, established tools such as Dinkelbach's algorithm provide effective power control mechanisms that enable adaptive resource allocation in dynamic CR environments. These optimization techniques reduce interference and help maintain the sharpness of transmitted thermal images.

Spectrum management that works well with machine learning improves channel selection in MIMO systems, which has a direct effect on image restoration. In massive MIMO systems, the pilot length is shorter than the number of antennas, which makes channel estimation quite difficult and results in pilot overhead. To address the issue, the proper selection of the estimator or optimization of the pilot length is important for the reconstructed model [8]. Transform-based and model-based approaches were used in earlier research on image restoration [9]. Wavelet transforms and spatial filtering are examples of classical methods that could remove noise but often failed to preserve fine structures, which results in important information being lost.

Transform-based and model-based methods were important in the past, but their inflexibility made them less popular. Changing to learning-based approaches, made possible by advancements in deep learning, facilitated restoration outcomes much better [9-13]. Nipuni Ginige et al. [14] utilized multi-layer Convolutional Neural Networks (CNNs) to identify the optimal channels for the transfer of large images. The result improved the transmission efficiency and made it less likely to be delayed. In a similar approach, Oktay et al. [15] developed their work using the Attention U-Net model, which used attention mechanisms to enhance segmentation, restoration, PSNR, and SSIM scores.

Similarly, Zhou et al. [16] implemented Nested U-Net (U-Net++) with densely connected skip paths to facilitate it easier to reuse features and preserve details, achieve PSNR values of 28–34 dB and SSIM values of 0.80 or higher. Rawat et al. [17] incorporated residual connections to U-Net topologies and addressed challenges that were presented from low-light and noisy situations, with PSNRs between 25 and 30 dB. Wang et al. [13] developed the Swin Transformer with multi-scale dependencies and obtained PSNRs between 34 and 37 dB. Gao et al. [18] investigated residual autoencoders and demonstrated they were effective in restoring missing or damaged regions, achieving PSNRs of up to 30 dB and SSIMs above 0.75. These frameworks improved image restoration, which made it possible to obtain back images of excellent quality even in adverse conditions. Despite these improvements, most studies concentrate merely on restoration algorithms and fail to connect them to thermal calibration,

spectrum management, or energy-efficient transmission. Most studies continue to concentrate solely on restoration methods, even with these advancements. They fail to relate them to temperature calibration, spectrum management, or energy-efficient transmission. Current research focuses on these aspects of isolation, which result in a lack of comprehensive frameworks that incorporate adaptive channel selection, efficient power management, and accurate image restoration. This gap needs to be resolved in order to build reliable wireless thermal image transmission systems that work in healthcare settings with restricted resources. It is vital that we minimize this gap so that we can create wireless thermal image transmission systems that operate well in healthcare settings with few resources.

To overcome the above challenges, this study introduces the TMCR framework, with the main contributions summarized below:

- To establish a TMCR framework, where a single thermal image is transmitted through an underlay cognitive MIMO system in a medical monitoring application.
- To propose an Opti-MSEEE algorithm with a closed-form mathematical model that jointly minimizes Sum-MSE and maximizes EE with superior performance compared to conventional methods.
- To achieve a dynamic channel selection mechanism, a CNN model was proposed for the CBS transmitter for optimal transmission path identification and energy-efficient thermal image delivery.
- To design a NAFNet-lite restoration model at the receiver for the accurate restoration of distorted images, comparative evaluation shows that the designed model performs better than Swin U-Net, U-Net, Residual U-Net, Transformer, and Wavelet Transformer approaches.
- To validate the TMCR framework experimentally through a Raspberry Pi 4 as CBS, a MIMO-enabled relay, and a smartphone-mounted thermal camera as the SU, demonstrating high-quality thermal image reconstruction and consistent temperature fidelity for diagnostic reliability.

The following sections are organized as follows: Section 3 presents the proposed system model and describes the first-hop, operation phases, and second-hop transmission. Section 4 formulates the optimization problem with its objectives and constraints. Sections 5 and 6 derive the minimum Sum-MSE and optimal power allocation to maximize EE using Lagrangian optimization, and Section 7 evaluates the performance of the proposed system model through the proposed Opti-MSEEE algorithm. Section 8 describes the hardware setup and illustrates the CNN-based channel selection model, thermal breast image restoration process, and different U-Net models' results, such as PSNR, SSIM, and temperature analysis. Section 9 concludes the paper, followed by references.

3. System Model for Thermal Image Transmission

Consider a Cell-free massive MIMO(CFmMIMO) underlay cognitive network with 'n' SUs randomly distributed within an area R as shown in Figure 1. The user-centric architecture consists of a CBS transmitter, equipped with N_t antennas and a secondary Amplify and Forward (AF) relay (S_{relay}) employing the MIMO technique. The S_{relay} is equipped with M (where $M > N_t$) the antennas that communicate to a single antenna terminal of SUs in full duplex mode. The network coexists with N_{PU} primary user transmitters (PU_{tx}), each having N_{PT} antennas. The relay R operates in full-duplex mode, forwarding data from CBS to the SUs. The channels from the CBS to the relay and from the relay to the SUs are assumed to experience independent frequency-flat Rayleigh fading. Moreover, mutual interference is present between the primary user receiver (PU_{rx}) and the SUs.

3.1. Transmission Model

In the proposed network, the information transmission is carried out over two sequential hops using generated Orthogonal Frequency Division Multiplexing (OFDM) subcarriers. In the first hop operation, the CBS performs spectrum sensing and transmits the information through an MIMO-OFDM link, where this information consists of a thermal image. In the second hop, the same information is then forwarded to the SUs.

3.1.1. First hop Transmission

In the initial hop, the CBS performs spectrum sensing, then transmits a thermal image over an MIMO-OFDM channel to the AF relay using N_{CBS} antennas across M subcarriers. Let τ_p and τ_d denote the durations allocated for pilot and thermal image transmission, respectively, with the total coherence time [19] given by $\tau_c = \tau_p + \tau_d$. The ratio τ_p/τ_d defines the pilot overhead, which reduces the effective time available for thermal image transmission. The received signal [20] at the j-th antenna of the optimal relay r_2 on the subcarrier m is expressed as in equation (1),

$$y_{m,r_2}^{(j)} = \sum_{\substack{j=1 \\ s=\tau_s,\tau_p,}}^{N_{CBS}} x_s(m)\, H_{s,j}^{(m)} \;+\; \sum_{u=1}^{N_u} \sqrt{P}\, x_u\, H_{u,r_2}^{(PU_{tx})} \;+$$

$$z_{j,r_2} \tag{1}$$

where $y_{m,r_2}^{(j)}$ denotes the received signal at the j-th antenna of r_2 on the m-th. The initial term represents the superposition of thermal images transmitted from the CBS antennas, where $\boldsymbol{p}_s(s,m)$ is the transmit power is allocated to the s-th antenna on the subcarrier.

During the channel estimation phase (τ_c), $s_s^{(m)} = s_{p,s}^{(m)}$ represents a known pilot symbol with unit average energy, i.e $\mathbb{E}\left[\left|s_{p,s}^{(m)}\right|^2\right] = 1$. Similarly, in the data transmission phase (τ_d), $s_s^{(m)} = s_{d,s}^{(m)}$ represents an information-bearing

data symbol (e.g., from the image stream), also normalized such that $\mathbb{E}\left[\left|s_{d,s}^{(m)}\right|^2\right] = 1$.

With transmit power allocation $p_s(s,m)$, the transmitted signal is defined as $x_s(m) = \sqrt{p_s(s,m)}s_s(m)$ and $H_{s,j}^{(m)}$ denotes the channel coefficient between the CBS antenna s and the j-th antenna of the optimal relay r_2.

The second term of equation (1) captures the aggregated interference from the PU_{tx}. $H_{u,r_2}^{(PU_{tx})}$ is the channel coefficient from u-th PU_{tx} to r_2. Each PU transmits with fixed power P.

The final term z_{j,r_2} represents Additive White Gaussian Noise (AWGN) at the optimal relay r_2, assumed to be independently and identically distributed with variance σ^2 and zero mean.

3.1.2. Relay Operation

The relay-assisted downlink secondary transmission operates in two phases: i) an Energy Harvesting (EH) phase and ii) a data transfer phase.

Accordingly, the total time slot T is partitioned into two non-overlapping intervals, θT for EH and $(1 - \theta)T$ reserved for data (thermal image) transmission, where $0 < \theta < 1$ represents the Time-Switching (TS) factor.

During the θT interval, the relay harvests Radio Frequency(RF) energy from the modulated signals transmitted by the CBS. In the remaining $(1 - \theta)T$ interval, the relay utilizes the harvested energy to forward the signal from the relay to the destination in the downlink, while sharing the same frequency band with the primary network.

The two operational phases are described as follows,

During the EH phase (θT), the relay harvests energy from the CBS transmission with power p_s. The harvested energy is denoted by E_{EH}, is obtained as,

$$E_{EH} = \eta\theta T\, p_s\, \mathbb{E}[Tr(H_m H_m^H)] \tag{2}$$

Where $\eta \in (0,1)$ denotes the RF-to-Direct Current (DC) conversion efficiency and operator $Tr(\cdot)$ quantifies the total received signal power aggregated across all relay antennas for the m-th subcarrier. Finally, H_m represent the MIMO channel matrix between the CBS and the relay.

After harvesting energy as defined in equation (2), the transmit power during the data transmission phase $(1 - \theta)T$ - is constrained by both the harvested energy and the interference threshold imposed by the PU network.
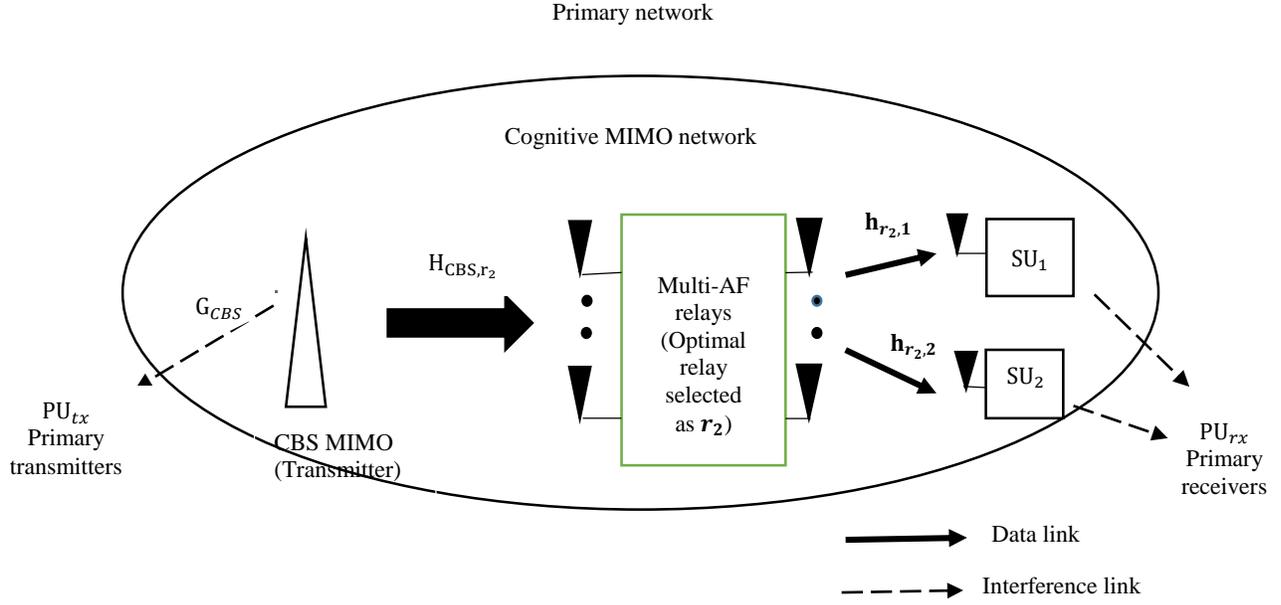
Primary network

Fig. 1 System model of CFmMIMO underlay cognitive network

The average power [21] available on subcarrier m is expressed as,

$$p_{n,r}(s,m) = min\left(\frac{E_{EH}}{(1-\theta)T.Tr(H_m H_m^H)}, \frac{I_{th}}{G_r(1-P_d)P_{PU}}\right) \qquad (3)$$

Where $Tr(H_m H_m^H)$ reflects the spatial channel gain on subcarrier m, I_{th} is the interference threshold at the PU_{rx}, G_r is the channel gain from the relay to the PUs, P_d is the probability of detection, and P_{PU} is the probability that the PU is active.

It is important to note that the relay executing the above operations is the optimal relay, determined using the Hybrid Partial Relay Selection (HPRS) method [22]. Since HPRS has been extensively discussed in the previously published work, HPRS emphasizes that the selected relay maximizes the minimum Signal to Noise Ratio (SNR) across the CBS to relay and relay to SU hops, ensuring both reliable channel estimation and energy-efficient forwarding of thermal images. Therefore, the achievable rate between the CBS transmitter and r_2 receiver during the first hop, is given as in equation (4),

$$R_1 = \left(1 - \frac{\tau_p}{\tau_c}\right)\frac{B}{M}\sum_{m=1}^{M} log_2\left(1 + SINR_{m,r_2}\right) \qquad (4)$$

Where $SINR_{m,r_2}$ denote the Signal-to-Interference-plus-Noise Ratio (SINR) on subcarrier m at the j–th antenna of r_2, given by the equation (5),

$$SINR_{m,r_2} = \frac{p_s(s,m)\left|\tilde{H}_{j,r_2}^{(m)}\right|^2}{\sum_{k\neq j,}^{N_{CBS}} p_s(s,k)\left|H_{k,r_2}^{(k)}\right|^2 + \sum_{u=1}^{U} P\left|H_{u,r_2}^{(PU tx)}\right|^2 + \sigma^2} \qquad (5)$$

Where $p_s(s,m)$ is the transmit power allocated by the CBS on subcarrier m, and $\tilde{H}_{j,r_2}^{(m)}$ is the effective MIMO coefficient between the CBS and the j-th received antenna of the r_2. The denominator accounts for the total interference and noise: the first term $\sum_{k\neq j,}^{N_{CBS}} p_s(s,k)\left|H_{k,r_2}^{(m)}\right|^2$ acquires co-channel interference from other CBS antennas, the second term $\sum_{u=1}^{U} P\left|H_{u,r_2}^{(PU tx)}\right|^2$ represents interference from PU_{tx} and σ^2 is the noise power at the optimal relay.

3.1.3. Channel Estimation and Data Transmission Over the Second Hop

After the EH process, the system proceeds to the channel estimation phase. In this phase, relay r_2 estimates the channels from the CBS by utilizing pilot symbols transmitted over a duration of $(1-\theta)T$. To obtain accurate channel estimations, a block-based pilot pattern is implemented. Each transmission frame has L_p consecutive pilot OFDM symbols, followed by L_d data symbols. Accordingly, the receiver adopts Linear Minimum Mean Square Error (LMMSE) [23] as a channel estimator for enhanced estimation accuracy. Consequently, to evaluate the sum rate in the second hop, the received images at the n-th SU on subcarrier m are modelled as in equation (6),

$$y_{n,m} = h_{n,m}\, x_R(s,m) + \sum_{g\neq n}^{N} h_{n,m}x_g + b_{n,m} + z_{n,m} \qquad (6)$$

Where $h_{n,m}$ denoted as the channel vector from the relay to the n-th SU on the subcarrier, $x_R(s,m)$ is the transmit vector from the relay, as $x_R(s,m) = \sum_{n=1}^{N} \sqrt{p_{nr}(s,m)}\, w_{n,m}x_{n,m}$, $w_{n,m}$ being the beamforming vector [29], and $x_{n,m}$ denoted as the information symbol for the n-th SU. The term $b_{n,m} = \sum_{s=1}^{S} H_{g,s}^{(PU rx)}$ represents aggregated interference from PU_{rx}, while the summation

$\sum_{g \neq n}^{N} h_{n,m} x_g$ accounts for inter-SU interference. The noise component $z_{n,m} ⊡$ XN $(0, \sigma_n^2)$ is denoted as AWGN. Thus, SINR at the n-th SU on subcarrier m is formulated as in equation (7).

$$SINR_{m,n} = \frac{|h_{n,m}|^2 |x_R(s,m)|^2}{\sum_{n \neq g}^{N} |h_{n,m}|^2 |x_g|^2 + |b_{n,}|^2 + \sigma_n^2 + I_s} \tag{7}$$

Where $x_R(s, m)$ is the transmit signal vector from the relay.

Finally, the second-hop sum rate R_2 is computed as,

$$R_2 = \left(1 - \frac{\tau_p}{\tau_c}\right) \frac{B}{M} \sum_{m=1}^{M} log_2\left(1 + SINR_{m,n}\right) \tag{8}$$

Where τ_p and τ_c denote the pilot duration and the channel coherence interval. Here, B denotes the total system bandwidth, and $B_m = \frac{B}{M}$ represents the bandwidth of each subcarrier. The term γ_n is the SINR for the n-th SU.

4. Problem Formulation within the System Model

Contribution 1: Minimization of $Sum - MSE_m$ for thermal image transmission

To minimize the channel estimation error, the pilot matrix X_m^p is designed through a Sum-MSE minimization problem subject to the transmit power limits of both CBS and the relay. Let p_s and p_r denote the transmit powers of the CBS and the optimal relay r_2 respectively, over subcarrier m.

The optimization problem is formulated as equation (9)

$$\min_{X_m^p} Sum - MSE \tag{9}$$

subject to $Tr\{E_s E_s^H Y_m\} \leq 2L_p p_s \tag{9a}$

$$Tr\{E_R E_R^H Y_m\} \leq 2L_p(1 - \theta)\eta p_r \tag{9b}$$

$$Y_m > 0 \tag{9c}$$

Where the Gram matrix $Y_m = \left(X_m^p\right)^H X_m^p$, L_p is the number of pilot OFDM symbols, and E_s, E_R are the source and relay selection matrices, respectively. The factor of 2 accounts for the In-phase and Out-phase (I/Q) components. Constraint (9a) limits the CBS pilot power, (9b) restricts the relay power based on harvested energy, and (9c) ensures that Y_m remains positive definite for a valid and stable solution.

Contribution 2: Joint Sum-MSE and EE optimization for quality-preserved thermal image transmission.

To achieve a balance between estimation error minimization and EE maximization, the optimal power allocation across sensing (p_{sense}), source (p_s), and relay (p_r) transmissions are formulated in equations (10)–(10c)

$$EE= \max_{P_T \leq P_{max}} \frac{max\{R_1, R_2\}}{p_{sense} + p_s + p_r} \tag{10}$$

subject to $p_s |G_{CBS}|^2 + p_r |G_{SU}|^2 \leq I_{th} \tag{10a}$

$$p_s + p_r + p_{sense} \leq p_{max} \tag{10b}$$

$$R_1, R_2 \geq R_{min} \tag{10c}$$

Equation (10) defines the EE as the maximum achievable rate per unit total power consumption, where the total transmit power (P_T) defined as constrained by the maximum power budget (p_{max}). Constraints (10a)–(10c) ensure that the interference threshold is not exceeded, the total power remains within the budget, and the minimum rate requirements are satisfied.

5. Derivation of Minimum SUM-MSE using Lagrangian Optimization

To obtain a closed-form solution for the Sum-MSE minimization problem, the problem is formulated as a convex optimization under the p_s, p_r and Y_m constraint. This problem is addressed using the proposed Lagrangian optimization, where the dual variables β_m, δ_m and μ_m [24] enforces the constraints associated with source power, relay, and matrix positivity.

The Lagrangian function is defined as in equation (11),

$$L(Y_m . \beta_m, \delta_m, \mu_m) = Tr\{B^{-2} Y_m^{-1}\} + \beta_m\left(Tr\{E_s E_s^H Y_m\} - 2L_p p_s\right) + \delta_r\left(Tr\{E_R E_R^H Y_m\} - 2L_p(1 - \theta)\eta p_r\right) - Tr\{\mu_r Y_m\} \tag{11}$$

Where $\beta_m \geq 0$, $\delta_m \geq 0$ and $\mu_m \geq 0$ are the Lagrange multipliers corresponding to the power constraints and the semi-definite condition on Y_m.

Based on the optimality conditions derived through the KKT framework, a closed-form expression for the minimum Sum-MSE [25] is given by equation (11),

$$Sum - MSE_m = \frac{2}{L_p}\left(\frac{1}{p_s} + \frac{1}{g^2 p_r}\right) \times Tr(C_w) \tag{12}$$

Where $Sum - MSE_m$ defined as the minimum estimation error, which depends on the pilot length L_p, source power (p_s), relay power (p_r), relay gain(g) and C_w is the channel correlation matrix.

6. Power Allocation Strategy for Sum-MSE Reduction and EE Maximization

In this section, the power allocation strategy is derived by minimizing the $Sum - MSE_m$ [25] subject to the total power constraints in equation(12).The problem is defined using a proposed Lagrangian-based optimization model, which captures the trade-off between estimation error reduction and total power consumption and is expressed as,

$$L(p_s, p_r, p_{sense}) = \frac{2}{L_P}\left(\frac{1}{p_s} + \frac{1}{g^2 \eta p_r}\right) + \zeta\left(p_s + p_r + p_{sense} - p_{max}\right) \tag{13}$$

Where ζ represents the Lagrange multiplier.

By applying the KKT optimality conditions to equation

(13), the closed-form power allocation values are derived. The optimal source and relay transmit powers are obtained as

$$p_s = \frac{p_{max}}{g\sqrt{\eta}+1} \qquad (14)$$

and

$$p_r = \frac{g\sqrt{n}p_{max}}{g\sqrt{\eta}+1} \qquad (15)$$

While the sensing power satisfies $p_{sense} = 0$, indicates the sensing power should be small but non-zero and bounded by the total available power.

Note: The complete mathematical derivation and extended analytical formulations of the proposed Opti-MSEEE algorithm have been communicated separately as a manuscript to the *Electrical Engineering* journal (Springer). Under this strategy, the proposed framework is summarized in Algorithm I, referred to as the Opti-MSEEE algorithm, which determines the optimal distribution of source, relay, and sensing powers to minimize the Sum-MSE while enhancing EE under the given system constraints.

Algorithm I: Optimized Sum-MSE and Energy Efficiency Enhancement (Opti-MSEEE)
#function   Opti-MSEEE(SNR_target,M,mod_scheme, θ,η,α, T β,P_d, τ_p, τ_c, p_{max},B)
Step 1: Initialize B, L_p , g _values,
Step 2: Generate binary data for thermal image
Step 3: Modulate data using mod_scheme
Step 4: Apply IFFT for OFDM and add cyclic prefix
Step 5: Calculate data rates for two hops
Calculate R₁ using Eq. (4)
Calculate R₂ using Eq. (8)
# Step 6: Optimization Loop
for g in g _values:
# Calculate EE
EE = f(R₁, R₂,p_{max} ,g) using Eq. (10)
# Calculate Sum MSE
Sum_MSE = calculate using Eq. (12)
# Multi-objective optimization
obj = α × Sum_MSE + β × (1/EE)
if obj < best_obj:
best_obj = obj
opt_MSE, opt_EE = Sum_MSE, EE
Step 7: Return opt_MSE, opt_EE
end function

7. Simulation Results and Discussion of Network Model

This section presents the simulation setup used to evaluate the performance of the proposed Opti-MSEEE algorithm for thermal image transmission over a MIMO-OFDM network. The scenario considers 10 SUs in an underlay CR environment, each assigned an energy budget of 10 mJ per 10-ms transmission slot at an RF power of 1 W, with a path loss exponent of 3.8.

Thermal images are transmitted using Quadrature Phase Shift Keying (QPSK) modulation over 5 or 10 subcarriers, with a total bandwidth of 100 MHz and a subchannel bandwidth of 6 MHz. The transmission power is fixed at 1W, while each node consumes 2mW of circuit power. These parameters provide a practical framework to assess the algorithm's ability to preserve image quality by sustaining high PSNR under channel noise and power constraints.
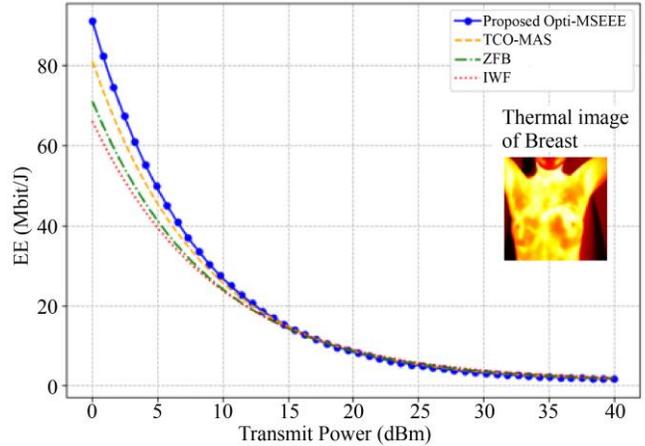

Fig. 2 Comparison of the proposed Opti-MSEEE with existing methods (TCO-MAS, ZFB, and IWF) for breast thermal image reconstruction

Figure 2 presents the comparison of EE between the proposed Opti-MSEEE and existing schemes: Termite Colony Optimization-based Multi-Agent System (TCO-MAS) [26], Zero Forcing Beamforming (ZFB) [27], and Interference Waveform Fluctuation (IWF) [28] across different transmit power levels (p_{max}) dBm. The proposed Opti-MSEEE algorithm consistently outperforms existing schemes, namely TCO-MAS, ZFB, and IWF.

At high transmit power (35–40 dBm), all methods converge to nearly the same values, with only a marginal difference of less than 0.5 Mbit/J. These results confirm the superiority of Opti-MSEEE, particularly in low- and medium-power regimes where EE is most critical for thermal image transmission.

In continuation, the Sum-MSE results are shown in Figure 3, the variation of Sum-MSE with SNR for different relay gains $g = \{1,5,15\}$ under both the proposed and equal power allocation schemes. The proposed method achieves lower Sum-MSE across all values of g by adaptively distributing source and relay powers, thereby reducing channel estimation error during thermal image transmission.

For a fixed SNR, the Sum-MSE increases with the larger relay gains due to noise amplification, with the lowest error at $g = 1$ and the highest at $g = 15$. All curves decrease with increasing SNR, confirming that higher SNR improves channel estimation accuracy and enhances thermal image transmission quality.
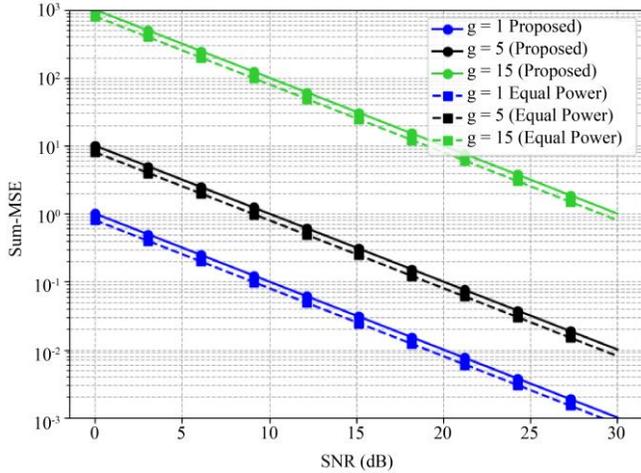
Fig. 3 Sum-MSE versus SNR (dB) for different relay gain factors (*g*) in the proposed Opti-MSEEE network suitable for breast thermal images

8. Hardware Setup for Validation

The hardware setup utilizes Raspberry Pi 4 (RPi4) modules programmed with the opti-MSEEE algorithm, optimal channel selection, and thermal image transmission. A total of three RPi4 units are configured for MIMO communication. One server unit operates as the transmitter with a 4×4 MIMO configuration using four Wi-Fi dongles and two receiver units, SU_1 and SU_2 are designated as the pathology and radiology labs, respectively. Each is configured as a 2×2 SU-MIMO with two Wi-Fi dongles and two receiver units SU_1 and SU_2 are designated as pathology and radiology labs, respectively.

The transmitter, programmed on RPi4, denoted as A, performs channel sensing, CNN-driven channel selection, and encrypted thermal image transmission using QPSK. At the receiver, a NAFNet-lite restoration module reduces channel-induced blur and noise and ensures reliable image recovery. The complete end-to-end workflow achieves an execution time of approximately 1seconds, as illustrated in Figures 4 and 5.

8.1. Operational Flow of the Proposed Hardware Setup
8.1.1. Thermal Image Acquisition
Infrared (IR) cameras are extensively used in medical thermography. FLIR models such as the FLIR T1020 and FLRSC620 [29] are well known for their reliability and sensitivity. In this study, thermal images of a bedridden patient were obtained from a thermography website [30]. The source provides clinically validated thermograms for diagnostic research.

8.1.2. Pre-Processing of Thermal Image
At the transmitter, each thermal image is pre-processed before wireless transmission. The step includes resizing to 128×128 pixels, normalization of pixel intensities, RGB conversion to represent thermal variations, and application of a Gaussian blur filter to suppress high-frequency noise and smooth details, which improves robustness during restoration. After pre-processing, a synthetic dataset is created by the addition of noise and blur to the clean images in order to simulate channel distortions. This dataset consists of paired samples, where each distorted thermal image is matched with its clean counterpart. A total of 500 image pairs [30, 31] are generated and loaded into a data loader with a batch size of 20. These pairs are then used during training of the NAFNet-lite and U-Net restoration models, which enable the networks to learn to restore high-quality thermal images from distorted thermal images.

8.1.3. Channel Selection and Transmission
The bit stream generated from the pre-processed thermal image is passed through a channel where the transmitting channel is selected using a CNN-based channel selection module. The parameters from the Opti-MSEEE algorithm include power, QPSK symbol mapping, Inverse Fast Fourier Transform (IFFT), and cyclic prefix insertion. Therefore, the Opti-MSEEE algorithm, channel sensing, Received Signal Strength Indicator (RSSI), noise-level, occupancy across the available Wi-Fi spectrum, and CNN module were programmed on the RPi 4.

Additionally, pilot symbols are embedded in each frame to enable accurate CSI estimation at the receiver. The transmission is carried out using four Wi-Fi dongles configured in a 4x4 MIMO arrangement on the RPi4.Each dongle operates on a distinct 2.4GHz (e.g., Channels 1, 6, 11, and 13) to establish parallel spatial links. The encoded bit streams are simultaneously transmitted to two receiver modules located at R_{x_1} and R_{x_2}.

This setup increases spectral utilization and ensures reliable thermal image delivery under variable network conditions. The CNN-based model processes real-time CSI, represented as a tensor (F, N_r, N_t, C) as shown in the Figure 6. The Massive MIMO spatial channel model dataset [31] was used to train the proposed model. It has realistic MIMO channel realizations with CSI, SNR, and spatial correlation matrices. The network consists of two convolutional layers (32 and 64 filters, 3×3 kernels) with Batch Normalization and ReLU activations, followed by global average pooling to summarize antenna-level features.

A dense layer with 128 neurons and dropout of 0.2 refines the representation, and a Softmax output layer assigns probability scores to available Wi-Fi channels. The channel with the highest score is then selected for transmission. The network is trained using the Adam optimizer ($\beta_1 = 0.9$, $\beta_2 = 0.999$) with an initial learning rate that gradually reduces to 3×10^{-5} through a cosine decay schedule following a five-epoch warm-up.
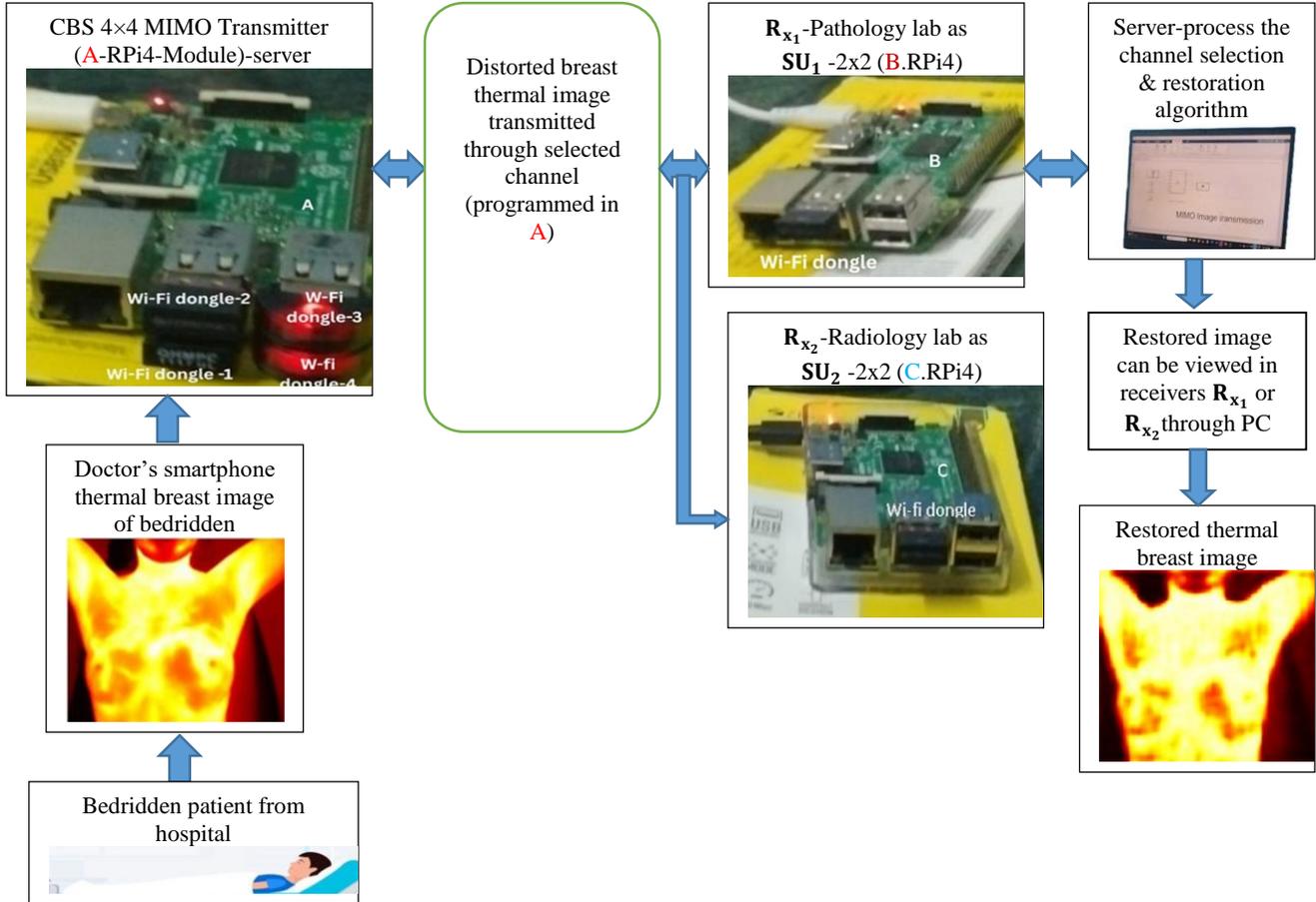
Fig. 4 Proposed experimental setup and system workflow for thermal image transmission and restoration process.
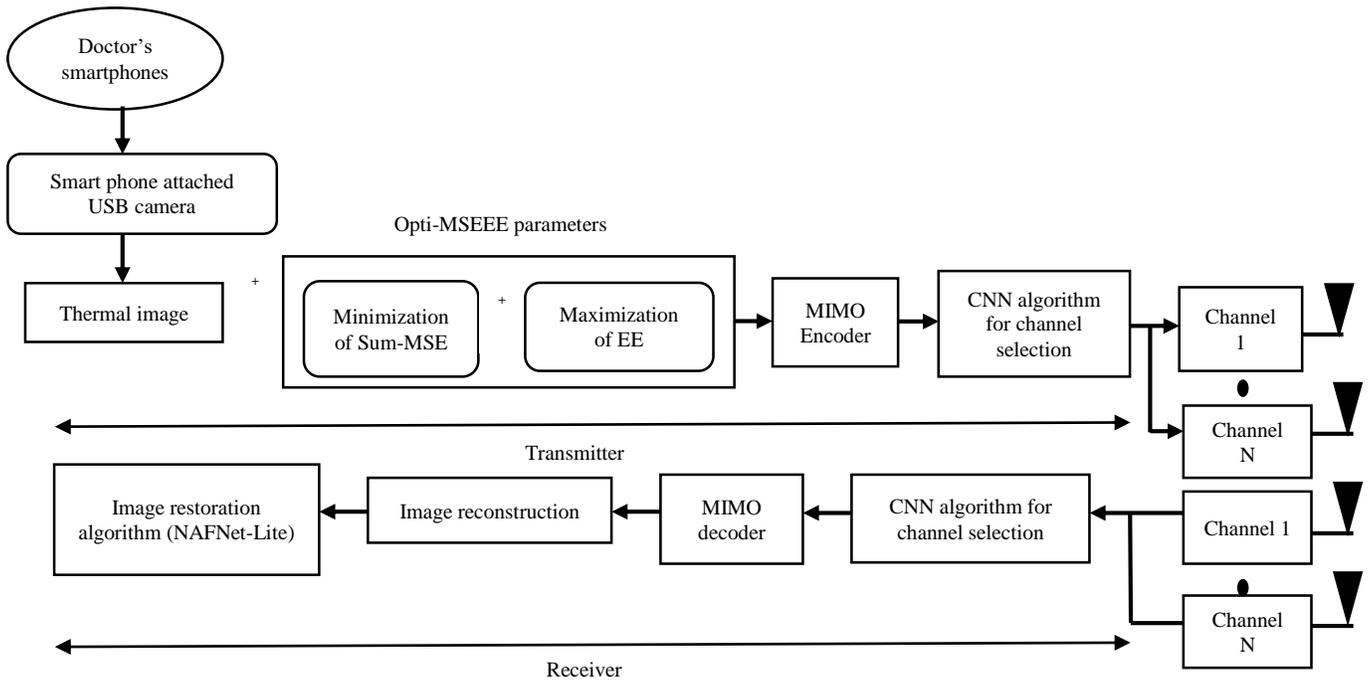

Fig. 5 Block diagram of the proposed experimental setup with thermal image transmission using QPSK modulation, MIMO channel, and CNN-based channel selection and restoration

The model is trained for 80 epochs with a batch size of 64, incorporating early stopping (patience = 10, minimum Δ = 0.002), weight decay of 1×10^{-4}, and gradient clipping with a global norm of 1 to stabilize optimization. To make the model more robust, Gaussian noise (σ = 0.02 relative to the CSI standard deviation) is added during training.
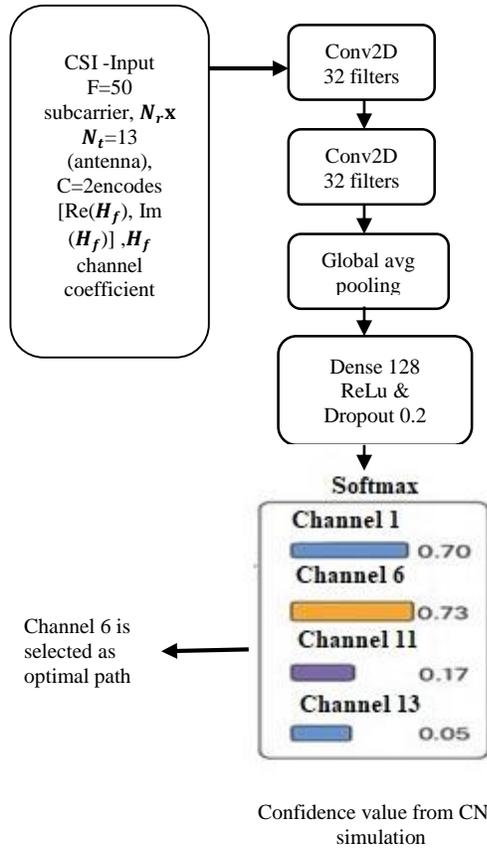

Fig. 6 CNN-based channel selection model at the transmitter and receiver end

8.1.4. Reception and Image Restoration

At the receiver, pilot symbols included in each frame serve as reference signals to estimate the channel. A Python module processes the transmitted data to create a CSI tensor with real and imaginary parts. The receiver uses this CSI to equalize and check the channel. Figure 7 illustrates the full process of the proposed NAFNet-lite architecture received through the MIMO channel. Figure 8 also provides a detailed view of the encoder and decoder functions.

Each block shows the following steps in order: convolution, Simplified Channel Attention (SCA), Simple Gate (SG) activation down-sampling, and up-sampling. After feature extraction, the lightweight NAF block in Layer-1 uses a 1×1 convolution for channel projection, an SG activation, and a depth-wise 3×3 convolution for spatial feature extraction. This process produces output features of size 128 × 128 × 32. Subsequently, the down-sampling stage starts with a stride-2 convolution, which reduces the spatial resolution to

64 × 64 and increases the channel depth to 64. Following down-sampling (encoder), a second NAF block in Layer 2 further improves the feature representation. Finally, the bottleneck stage increases the channel depth to 128, allowing for more detailed features.

In continuation of this, the up-sampling stage (decoder) employs a transposed convolution to restore the spatial resolution from 64×64 back to 128×128 and reduce the channel depth to 32. Finally, the reconstruction stage applies a 3×3 convolution to generate the restored thermal image of size 128×128×3. For training, a dataset of 300 paired distorted and clean thermal images was constructed. The clean images were first prepared and then transmitted through the simulated MIMO-OFDM channel to obtain the distorted images. Using these pairs, the training process optimizes the entire architecture, not just one stage, ensuring that the parameters across all layers are updated for effective image restoration. To increase robustness, the dataset was expanded into thousands of samples using patch extraction and data augmentation, while regularization strategies such as dropout and early stopping were applied to improve generalization. To evaluate different restoration strategies, multiple deep learning models were simulated on the prepared dataset. Table 1 summarizes the simulated model, its architectural descriptions, and the proposed training Hyperparameters employed in the experiments.

8.2. Experimental Evaluation

All U-net models were trained and evaluated using the same dataset of breast thermal images to ensure a fair comparison. During evaluation, the distorted test images were passed through each model to obtain the restored outputs. Performance was assessed using the PSNR and SSIM by measuring the maximum (max) and minimum (min) temperature values from the restored thermal images. These measurements provide a practical indication of each model's ability to preserve critical thermal information relevant for diagnostic analysis.

The restored thermal images from various deep learning models, as listed in Table 1, were evaluated using PSNR and SSIM to determine overall reconstruction quality. This evaluation created a consistent framework for linking restoration models to temperature-based analysis using the dataset [30, 31]. Specifically, the analysis focused on the left Region of Interest (ROI) of the breast thermal image, which corresponds to the patient's left breast. Intensity temperature mapping and the dataset's reference temperature information were used to calculate the max and min temperatures within the left ROI for each restored breast image. The left ROI-based thermal evaluation from the dataset improves the clinical value of PSNR and SSIM analyses. To address age-related differences in breast thermography, the dataset has been organized into five age batches: under 30, 31 to 40, 41 to 50, 51 to 60, and over 60 years.
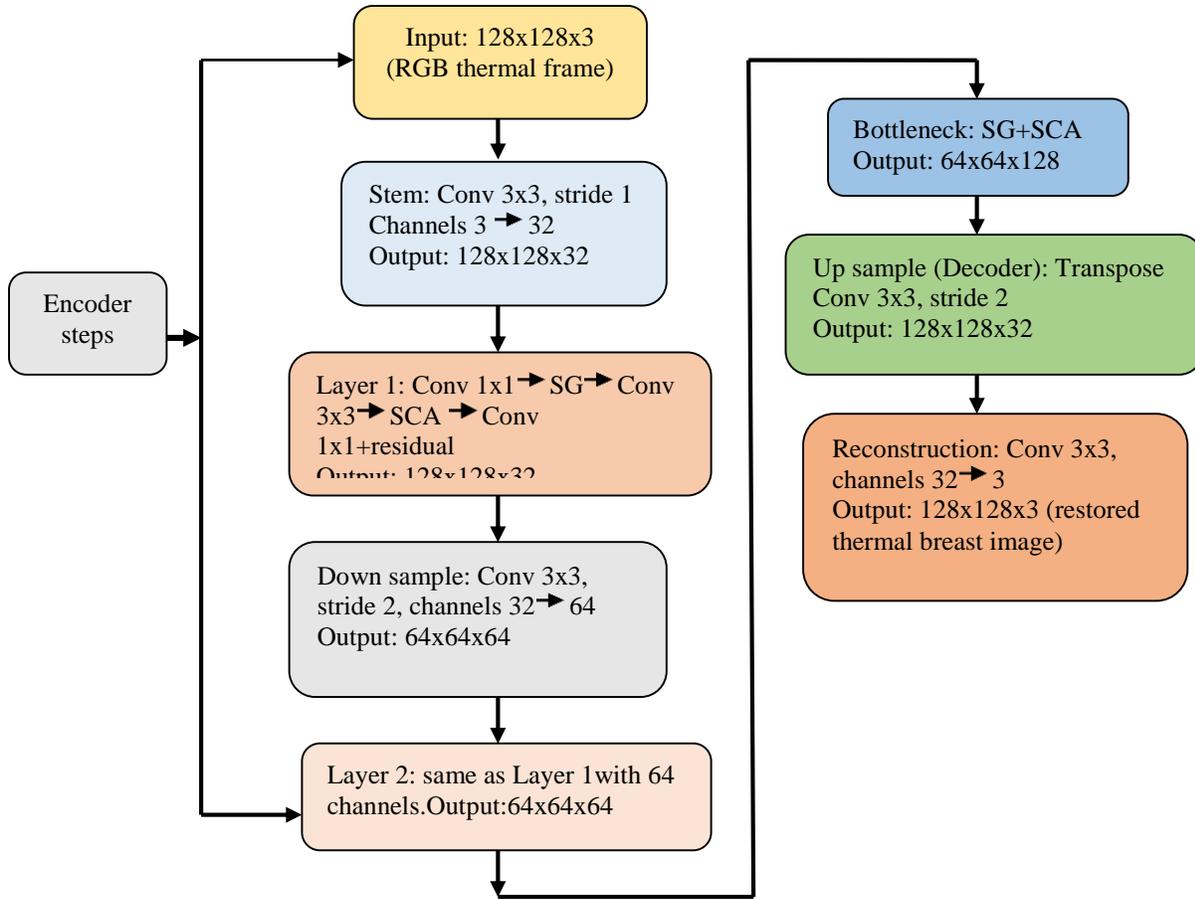
Fig. 7 Restoration model for a single thermal image of the proposed NAFNet-lite model.

Table 1. Overview of simulated model architectures and unified training settings

Simulated Model	Description	Proposed Hyperparameters
Swin U-Net [32]	CNN layers + GELU	a.Learning rate: 1e-4 b.Optimizer: Adam c.Loss:MSE d.Epochs:800 e.Batch size 20 f.Padding: 1 g.Nomarmalization: Batch h.Kernel size:3x3 i.Stride:2
U-Ne t [33]	Encoder & decoder with pooling and skip connections.	
Residual U-Net [34]	U-Net backbone augmented with residual blocks with transpose convolutions	
NAF-Net lite (proposed) [35]	Nonlinear Activation Free (NAF) blocks, stem, and transpose convolution	
Transformer [36]	Shallow CNN with ReLU	
Wavelet Transformer [37]	Convolutional layers with wavelet decomposition	

a.Source image   b.Pre-processing image   c.Distorted image

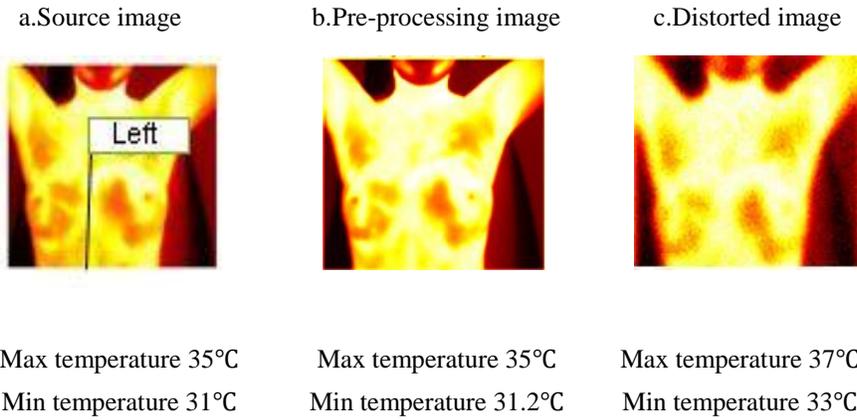| Max temperature 35℃ | Max temperature 35℃ | Max temperature 37℃ |
| Min temperature 31℃ | Min temperature 31.2℃ | Min temperature 33℃ |

Fig. 8 Temperature variations of the left ROI across: original, pre-processed, and distorted thermal image

Table 2. Comparative analysis of different deep learning models based on PSNR, SSIM, and left ROI temperature measurements for restored breast thermal images

Simulated models	Restored breast thermal image	Left ROI (temperature)	SSIM	Simulated models	Restored breast thermal image	Left ROI (temperature)	SSIM
Swim U-Net	PSNR:29.2dB	Max:36.2℃ Min:33.4℃	0.769	NAF-Net lite	PSNR:31.2dB	Max:34.8℃ Min:31.3℃	0.794
U-Net	PSNR:27.6dB	Max:34.5℃ Min:32. 3℃	0.735	Transfo-rmer	PSNR:30dB	Max:36℃ Min:33.4℃	0.780
Residual U-Net	PSNR:28.4dB	Max:33.8. ℃ Min:32.1℃	0.744	Wavelet Transfor-mer	PSNR:29dB	Max:36.1℃ Min:33.6℃	0.770

From each batch, the patients' ages were used to find the reference temperature and calculated as the average of the highest and lowest temperatures in the thermal breast images. Further, the left ROI temperature readings have been compared with the age-specific body temperature ranges for accurate and reliable diagnosis.

Figure 8 illustrates the temperature changes in the left ROI between the original, pre-processed, and distorted thermal image. The original image had a constant temperature range of 31–35 °C, which remained unchanged upon pre-processing. However, transmission through the MIMO channel reached both the highest and lowest temperatures (37 °C and 33 °C, respectively) due to fading and noise effects. This shows that the thermal distribution was degraded. Subsequently, Table 2 presents a related analysis that evaluates the performance of the restoration models using PSNR, SSIM, and left ROI temperature values. The proposed NAFNet-Lite model represents the highest PSNR (31.2 dB) and SSIM (0.794), and maintains the temperatures closest to the original, with small changes in the maximum (34.8 °C) and minimum (31.3 °C) values.

Compared to the proposed approach, the other models demonstrate considerable temperature deviations, which are reflected in their corresponding PSNR and SSIM values. PSNR, in particular, is highly sensitive to intensity distortions caused by Gaussian noise and therefore serves as an effective metric for evaluating pixel-level reconstruction fidelity. In this study, temperature variations are quantitatively analyzed by mapping temperature differences to pixel intensity values. The minimum and maximum pixel intensities represent the lowest and highest temperature points within the selected region, respectively. Since pixel intensities are directly correlated with temperature values [38], accurate image reconstruction is critical for preserving clinically relevant information.

To assess reconstruction performance, pixel-wise intensity differences [39] between the degraded and reconstructed images are examined to determine how effectively the proposed NAFNet-lite and the comparative models recover the original intensity distributions. Both proposed NAFNet-Lite and U-Net models significantly reduce intensity distortions introduced by channel impairments, particularly in regions corresponding to extreme low and high temperatures, resulting in reconstructed thermal images that closely match the original thermal distribution. Accurate recovery of pixel intensities improves local contrast and preserves fine temperature gradients, thereby enhancing the reliability of subsequent diagnostic evaluations. However, continuous monitoring of temperature variations within the ROI enables early detection of abnormalities and supports timely clinical decision-making.

9. Conclusion

This work presents a Thermal Image Cognitive Radio (TMCR) framework for monitoring bedridden patient temperatures. It combines underlay cognitive MIMO transmission with deep learning-based image restoration. The proposed Opti-MSEEE algorithm minimizes Sum-MSE and maximizes EE under interference constraints. Simulation results show improved EE over existing methods. A CNN-driven channel selection mechanism, with a lightweight NAFNet-lite model, achieves 31.2 dB PSNR and 0.794 SSIM. The complete system was implemented with an end-to-end latency of one second on a Raspberry Pi test bed. The framework operates with a total of 120 ms to select a channel, 200 ms for transmission, 150 ms to estimate the channel, and 530 ms to restore the thermal image. The proposed model supports simultaneous monitoring of multiple patients through additional receiver units and maintains the thermal accuracy needed for clinical diagnosis. For healthcare to function well, deployment problems like RF calibration, clock synchronization, and interference management had to be solved. Due to high interference in a highly dense network, it leads to increased latency. Future study will focus on interference, other anatomical thermal areas in the database, and utilize radiometric data to improve diagnostic accuracy.

Acknowledgments

References

[1] G. Premalatha, and V. Thulasi Bai, "Design and Implementation of Intelligent Patient in-House Monitoring System based on Efficient XGBoost-CNN Approach," *Cognitive Neurodynamics*, vol. 16, pp. 1135-1149, 2022. [CrossRef] [Google Scholar] [Publisher Link]

[2] David Gertsvolf et al., "A U-net Convolutional Neural Network Deep Learning Model Application for Identification of Energy Loss in Infrared Thermographic Images," *Applied Energy*, vol. 360, pp. 1-15, 2024. [CrossRef] [Google Scholar] [Publisher Link]

[3] Himanshu Singh, and Millie Pant, "Auto-Minimum Resolvable Temperature Difference Method for Thermal Imagers," *Journal of Optics*, vol. 50, pp. 689-700, 2021. [CrossRef] [Google Scholar] [Publisher Link]

[4] S. Esakki Rajavel et al., "Energy Efficient Relay Selection Framework for 5G Communication using Cognitive Radio Networks," *Scientific Reports*, vol. 15, pp. 1-12, 2025. [CrossRef] [Google Scholar] [Publisher Link]

[5]   Umar Ghafoor, and Adil Masood Siddiqui, "Maximizing Energy Efficiency in 6G Cognitive Radio Network," *Digital Communications and Networks*, vol. 11, no. 5, pp. 1356-1369, 2025. [CrossRef] [Google Scholar] [Publisher Link]

[6]   Jianbin Liao et al., "Correction: Optimal Resource Allocation Method for Energy Harvesting Based Underlay Cognitive Radio Networks," *Plos one*, vol. 18, no. 1, 2023. [CrossRef] [Google Scholar] [Publisher Link]

[7]   Ramnaresh Yadav, Keshav Singh, and Ashwani Kumar, "Optimal Power Allocation for Achieving Secure Green Cognitive Radio Networks," *Electronics*, vol. 11, no. 13, pp. 1-19, 2022. [CrossRef] [Google Scholar] [Publisher Link]

[8]   Kai Zhang et al., "Learning Deep CNN Denoiser Prior for Image Restoration," *Proceedings of the IEEE Conference on Computer Vision and Pattern Recognition (CVPR)*, pp. 3929-3938, 2017. [Google Scholar] [Publisher Link]

[9]   Guanyu Liu et al., "A Lightweight Convolutional Network based on Pruning Algorithm for Yolo," *Fourteenth International Conference on Graphics and Image Processing (ICGIP 2022)*, vol. 12705, pp. 302-311, 2023. [CrossRef] [Google Scholar] [Publisher Link]

[10]   Ruiheng Zhang et al., "Graph-Based Few-Shot Learning with Transformed Feature Propagation and Optimal Class Allocation," *Neurocomputing*, vol. 470, pp. 247-256, 2022. [CrossRef] [Google Scholar] [Publisher Link]

[11]   Kai Zhang et al., "Beyond a Gaussian Denoiser: Residual Learning of Deep CNN for Image Denoising," *IEEE Transactions on Image Processing*, vol. 26, no. 7, pp. 3142-3155, 2017. [CrossRef] [Google Scholar] [Publisher Link]

[12]   Kai Zhang, Wangmeng Zuo, and Lei Zhang, "FFDNet: Toward a Fast and Flexible Solution for CNN-Based Image Denoising," *IEEE Transactions on Image Processing*, vol. 27, no. 9, pp. 4608-4622, 2018. [CrossRef] [Google Scholar] [Publisher Link]

[13]   Zhendong Wang et al., "Uformer: A General U-Shaped Transformer for Image Restoration," *Proceedings of the IEEE/CVF Conference on Computer Vision and Pattern Recognition (CVPR)*, pp. 17683-17693, 2022. [Google Scholar] [Publisher Link]

[14]   Nipuni Ginige et al., "Efficient Channel Prediction for Beyond Diagonal RIS-Assisted MIMO Systems With Channel Aging," *IEEE Transactions on Vehicular Technology*, vol. 74, no. 8, pp. 12658-12672, 2025. [CrossRef] [Google Scholar] [Publisher Link]

[15]   Ozan Oktay et al., "Attention U-Net: Learning Where to Look for the Pancreas," *arXiv preprint*, pp. 1-10, 2018. [CrossRef] [Google Scholar] [Publisher Link]

[16]   Zongwei Zhou et al., "UNet++: A Nested U-Net Architecture for Medical Image Segmentation," *Deep Learning in Medical Image Analysis and Multimodal Learning for Clinical Decision Support*, Granada, Spain, pp. 3-11, 2018. [CrossRef] [Google Scholar] [Publisher Link]

[17]   Siddharth Rawat., "*Holographic Microscopy of Complex Fluids*," PhD Thesis, University of New South Wales (Australia), pp. 1-171, 2023. [CrossRef] [Google Scholar] [Publisher Link]

[18]   Xinyi Gao, "*A Method for Face Image Inpainting Based on Generative Adversarial Networks*," PhD Dissertation, Auckland University of Technology, New Zealand, pp. 1-95, 2022. [Google Scholar] [Publisher Link]

[19]   Emil Björnson, Jakob Hoydis, and Luca Sanguinetti, "Massive MIMO Networks: Spectral, Energy, and Hardware Efficiency," *Foundations and Trends® in Signal Processing*, vol. 11, no. 3-4, pp. 154-655, 2017. [CrossRef] [Google Scholar] [Publisher Link]

[20]   Mahmoud Zaher et al., "Learning-Based Downlink Power Allocation in Cell-Free Massive MIMO Systems," *IEEE Transactions on Wireless Communications*, vol. 22, no. 1, pp. 174-188, 2023. [CrossRef] [Google Scholar] [Publisher Link]

[21]   Huan Zhang et al., "Rate Maximization of Wireless-Powered Cognitive Massive MIMO Systems," *IEEE Internet of Things Journal*, vol. 8, no. 7, pp. 5632-5644, 2020. [CrossRef] [Google Scholar] [Publisher Link]

[22]   Neji Mensi, and Danda B. Rawat, "On the Performance of Partial RIS Selection vs. Partial Relay Selection for Vehicular Communications," *IEEE Transactions on Vehicular Technology*, vol. 71, no. 9, pp. 9475-9489, 2022. [CrossRef] [Google Scholar] [Publisher Link]

[23]   Mohamed A. Abdel-Moneim et al., "CNN-Based Modulation Classification using Image Processing Techniques for OFDM Underwater Acoustic Communication System," *Journal of Electrical Systems and Information Technology*, vol. 12, pp. 1-29, 2025. [CrossRef] [Google Scholar] [Publisher Link]

[24]   Jin Wang et al., "Pilot Optimization and Power Allocation for OFDM-Based Full-Duplex Relay Networks with IQ-Imbalances," *IEEE Access*, vol. 5, pp. 24344-24352, 2017. [CrossRef] [Google Scholar] [Publisher Link]

[25]   Xingxiang Peng, Peiran Wu, and Minghua Xia, "Optimization for Multicarrier MIMO SWIPT Systems under MSE QoS Constraint," *2020 IEEE 91st Vehicular Technology Conference (VTC2020-Spring)*, Antwerp, Belgium, pp. 1-5, 2020. [CrossRef] [Google Scholar] [Publisher Link]

[26]   R. Kanmani, and S. Mary Praveena, "Bio Inspired Multi Agent System for Distributed Power and Interference Management in MIMO OFDM Networks," *Scientific Reports*, vol. 15, pp. 1-25, 2025. [CrossRef] [Google Scholar] [Publisher Link]

[27]   H. Yu et al., "Regularized Zero-Forcing Aided Hybrid Beamforming for Millimeter-Wave Multiuser MIMO Systems," *IEEE Transactions on Wireless Communications*, vol. 22, no. 5, pp. 3280-3295, 2022. [CrossRef] [Google Scholar] [Publisher Link]

[28]   Zhangliang Chen, "*Power Allocation and Massive Mimo Channel Modeling for 5G Wireless Communications*," Dissertation University of Texas at Arlington, pp. 1-121, 2022. [Google Scholar] [Publisher Link]

[29] Nasim Reza et al., "Thermal Imaging and Computer Vision Technologies for the Enhancement of Pig Husbandry: A Review," *Journal of Animal Science and Technology*, vol. 66, no. 1, pp. 31-56, 2024. [CrossRef] [Google Scholar] [Publisher Link]

[30] J. Zuluaga-Gomez et al., "A CNN-based Methodology for Breast Cancer Diagnosis using Thermal Images," *Computer Methods in Biomechanics and Biomedical Engineering: Imaging & Visualization*, vol. 9, no. 2, pp. 131-145, 2021. [CrossRef] [Google Scholar] [Publisher Link]

[31] L.A. Bezerra et al., "An Empirical Correlation to Estimate Thermal Properties of the Breast and of the Breast Nodule using Thermographic Images and Optimization Techniques," *International Journal of Heat and Mass Transfer*, vol. 149, 2020. [CrossRef] [Google Scholar] [Publisher Link]

[32] Massive MIMO Spatial Channel Model Dataset, Qualcomm Developer Network. [Online]. Available: https://www.qualcomm.com/developer/software/massive-mimo-spatial-channel-model-dataset

[33] Hu Cao et al., "Swin-Unet: Unet-Like Pure Transformer for Medical Image Segmentation," *Computer Vision – ECCV 2022 Workshops*, Tel Aviv, Israel, pp. 205-218, 2023. [CrossRef] [Google Scholar] [Publisher Link]

[34] Yaopeng Peng, Danny Z. Chen, and Milan Sonka, "U-Net V2: Rethinking the Skip Connections of U-Net for Medical Image Segmentation," *2025 IEEE 22nd International Symposium on Biomedical Imaging (ISBI)*, Houston, TX, USA, pp. 1-5, 2025. [CrossRef] [Google Scholar] [Publisher Link]

[35] Agnesh Chandra Yadav, Maheshkumar H. Kolekar, and Mukesh Kumar Zope, "Modified Recurrent Residual Attention U-Net Model for MRI-based Brain Tumor Segmentation," *Biomedical Signal Processing and Control*, vol. 102, 2025. [CrossRef] [Google Scholar] [Publisher Link]

[36] Giuseppe Nunnari, and Sonia Calvari, "Exploring Vision Transformers and Convolution Neural Networks for the Thermal Image Classification of Volcanic Activity," *Applied Sciences*, vol. 15, no. 5, pp. 1-18, 2025. [CrossRef] [Google Scholar] [Publisher Link]

[37] Houssem Habbouche et al., "A Wavelet Transform-Based Transfer Learning Approach for Enhanced Shaft Misalignment Diagnosis in Rotating Machinery," *Electronics*, vol. 14, no. 2, pp. 1-18, 2025. [CrossRef] [Google Scholar] [Publisher Link]

[38] Dario Scilla et al., "Computer Vision Corrections Enhance UAV-Based Retrievals in Shallow Waters," *IEEE Journal of Selected Topics in Applied Earth Observations and Remote Sensing*, vol. 18, pp. 18134-18149, 2025. [CrossRef] [Google Scholar] [Publisher Link]

[39] Tomas Vicar et al., "Cell Segmentation Methods for Label-free Contrast Microscopy: Review and Comprehensive Comparison," *BMC Bioinformatics*, vol. 20, pp. 1-25, 2019. [CrossRef] [Google Scholar] [Publisher Link]